Geochimica et Cosmochimica Acta 421 (2026) 342–355

Contents lists available at ScienceDirect

Geochimica et Cosmochimica Acta

journal homepage: www.elsevier.com/locate/gca

Neodymium stable isotope fractionation in minerals: Implications for Earth's differentiation, and planetary formation

Mark Nestmeyer [a,b,*], Alex J. McCoy-West [a,c]

[a] IsoTropics Geochemistry Laboratory, Earth and Environmental Science, James Cook University, Townsville, QLD 4811, Australia
[b] CSIRO Mineral Resources, Kensington, WA 6151, Australia
[c] Economic Geology Research Centre, James Cook University, Townsville, QLD 4811, Australia

ARTICLE INFO

Associate editor: Marc Blanchard

Keywords:
Stable isotope fractionation
Density functional theory
Nuclear field shift
Planetary differentiation
Igneous processes

ABSTRACT

The application of rare Earth element stable isotope compositions has become of increasing interest in geochemistry. Recently, studies have begun exploring variations in the stable $^{146}Nd/^{144}Nd$ isotope ratio in geological samples, with limited isotope fractionation observed in igneous rocks but significantly larger fractionations seen in low temperature systems. Experimental and theoretical studies on the equilibrium isotope fractionation of Nd are widely missing which can support understanding the fractionation of Nd isotopes among Earth's major reservoirs. Here, we have modelled the isotope fractionation factors for 15 common rock forming and accessory minerals to help understand equilibrium stable isotope fractionation during medium to high temperature processes.

We estimate that mantle melting will produce minimal isotope fractionation while the residual peridotite ought to retain heavier Nd isotopes which could explain a potentially superchondritic composition of the depleted mantle. This can be predicted because in mantle minerals with Mg sites (e.g. olivine, orthopyroxene) substitution of isotopically heavier Nd is preferred compared to minerals with Ca sites (e.g. clinopyroxene), with the latter being the major contributor to basaltic melts. The Earth's outer core (i.e. sulfide matte) is a potential host of lighter Nd isotopes which we demonstrate favours sulfides over silicates. However, the low partition coefficients of rare Earth elements into the core leads to a composition of the bulk silicate Earth that is indistinguishable from chondrites. A better understanding of the $\delta^{146/144}Nd$ composition of the mantle is warranted to elucidate the isotope fractionation of Nd between Earth's major geochemical reservoirs.

As Nd condenses from the solar nebular gas into primitive material, the mass-independent nuclear field shift effect dominates equilibrium isotope fractionation and produces significant fractionation in $\delta^{146/144}Nd$ even at high temperatures (>1000 °C) with the condensed material enriched in lighter Nd isotopes. However, the isotopic compositions reported for refractory inclusions (–1.86 to 2.20 ‰; Hu et al. (2021)) cannot be solely explained by equilibrium isotope fractionation and other mechanisms are required.

1. Introduction

The application of the radiogenic $^{143}Nd/^{144}Nd$ isotope ratio has a long tradition in geoscience for understanding planetary formation and elemental cycling between Earth's major reservoirs (de La Rocha et al., 1997; DePaolo, 2012; Piepgras and Wasserburg, 1980; Zindler and Hart, 1986). Stable isotopes of Nd, however, can potentially be used as an additional tracer of geochemical processes. The improving sensitivity of mass spectrometers allows us to measure stable isotope ratios of lanthanides with high precision (2SD < 0.05 ‰; Bai et al. (2023a), Bai et al. (2022), Liu et al. (2023b), Kaufmann and McCoy-West (2025), Nicol et al. (2023), McCoy-West et al. (2017), Wu et al. (2024)). Stable isotope ratios of Nd can be measured simultaneously with the long-established radiogenic $^{143}Nd/^{144}Nd$ ratio using a double spike and can additionally be collected with Sm in ion-exchange chromatography for geochronology (Liu et al., 2023a; McCoy-West et al., 2020b). The $^{146}Nd/^{144}Nd$ isotope ratio has been mostly reported in previous studies with isotopic data of a substance reported relative to the JNdi-1 standard in δ-notation:

* Corresponding author at: IsoTropics Geochemistry Laboratory, Earth and Environmental Science, James Cook University, Townsville, QLD 4811, Australia.
E-mail address: mark.nestmeyer@my.jcu.edu.au (M. Nestmeyer).

https://doi.org/10.1016/j.gca.2026.03.022
Received 28 August 2025; Accepted 10 March 2026
Available online 16 March 2026

$$\delta^{146}Nd = \left[\left(\frac{\frac{^{146}Nd}{^{144}NdSample}}{\frac{^{146}Nd}{^{144}NdJNdi-1}} \right) - 1 \right] \times 10^3 \quad (1)$$

The isotope fractionation between two Nd-bearing phases A, and B is then expressed in Δ-notation:

$$\Delta^{146}Nd_{A-B} = \delta^{146}Nd_A - \delta^{146}Nd_B \quad (2)$$

In terrestrial environments, Nd occurs only in the 3+ oxidation state which reduces the potential equilibrium fractionation between Nd-bearing phases. In high temperature systems, mass-dependent fractionation of heavy elements like Nd (Z = 60) will be limited because isotope fractionation diminishes with increasing temperature and atomic mass (Bigeleisen and Mayer, 1947). Therefore, equilibrium fractionation of Nd isotopes is likely to be more significant in low and intermediate temperature environments such as natural waters, metamorphic fluids or hydrothermal systems (Hu et al., 2023b; Nestmeyer and McCoy-West, 2025) where it is a potentially useful proxy due to its fluid immobility (Ayers et al., 1997).

The refractory and lithophile behaviour of Nd makes it useful for elucidating the geochemical evolution of planets but the debate surrounding the origin of Earth's Nd isotope anomalies, and whether its composition is chondritic, remains ongoing (Bouhifd et al., 2015; Boyet et al., 2018; Frossard et al., 2022). The study by McCoy-West et al. (2017) has shown that various chondrite types show a homogeneous composition of δ^{146}Nd = –0.027 ± 0.005 ‰ and global basalts closely resemble this value. Also, variations in igneous rocks are rather small (–0.054 to 0.022 ‰; McCoy-West et al. (2021)), and substantial deviations are most likely related to disequilibrium diffusion processes (–0.127 ‰; McCoy-West et al. (2020a)). Larger variations have been found in low temperature systems. Bai et al. (2025) found heavier δ^{146}Nd values of up to 0.114 ‰ in phosphates in seafloor sediments while substantially lighter values have been measured in weathering profiles (–0.207 ‰; Bai et al. (2023b)).

For heavy elements like rare Earth elements (REE), equilibrium fractionation during oxidation is heavily influenced by the mass-independent nuclear field shift (NFS) effect which enriches the isotope with greater volume in the lower oxidation state when electrons from p, d, or f- orbitals are removed (Bigeleisen, 1996) which is the case for the oxidation of lanthanides from 2+ to 3+, and 3+ to 4+. This contrasts with mass-dependent fractionation which usually enriches the more massive isotope in the higher oxidation state (Schauble, 2004). This has been demonstrated for the redox-sensitive lanthanides Ce (3+ to 4+) and Eu (2+ to 3+) where the field shift can cancel or dominate the isotope fractionation in redox reactions (Nestmeyer and McCoy-West, 2025; Schauble, 2023; Schauble, 2024). Neodymium can only occur in multiple oxidation states (0, 2+, 3+) during planetary formation. For example, in the solar nebular, Nd is present as NdO molecules and undergoes a change in oxidation state to 3+ during condensation of the nebular gas into primitive material and incorporation into minerals like perovskite or hibonite (Davis and Grossman, 1979; Sossi and Fegley Jr, 2018). Furthermore, given that mass-dependent fractionation is nearly proportional to $1/T^2$ versus NFS effect which is proportional to 1/T (Bigeleisen, 1996), at elevated temperatures prevailing in the solar nebula, equilibrium fractionation during oxidation is potentially dominated by the NFS effect.

To date, experimental studies that quantify isotope fractionation between Nd-bearing phases are extremely sparse with only a single study on fractionation between Nd in aqueous solution and surface complexes on Fe- and Mn-oxyhydroxides available (Nakada et al., 2013). Saji et al. (2016) observed mass-independent isotope fractionation of Nd in ion-exchange chromatography and attributed it to the nuclear field shift effect, but its significance for natural samples remains unknown. Here, we performed theoretical *ab initio* calculations of 15 Nd minerals relevant to igneous processes, and planetary formation to model and quantify both the mass-dependent and NFS component of the equilibrium fractionation between various phases and oxidation states. This study provides a framework that can be used in future studies to interpret natural variations of stable Nd isotope signatures.

2. Methodology

2.1. Mass-dependent fractionation

Reduced partition function ratios ($10^3 \ln\beta_{MD}$) of Nd phases were calculated from first principles. β-factors represent the isotope fractionation of a phase relative to an atomic vapor of Nd. The difference in isotopic composition between two phases A, and B (α-factor) is calculated by:

$$10^3 ln\alpha_{A-B} = 10^3 ln\beta_A - 10^3 ln\beta_B \quad (3)$$

which corresponds to the difference in isotopic composition between species A, and B with the isotopic composition of A, and B measured relative to a widely used reference material:

$$10^3 ln\alpha_{A-B} \approx \Delta^{146}Nd_{A-B} \quad (4)$$

Reduced partition function ratios ($10^3 \ln\beta_{MD}$) of minerals and molecules were computed in CRYSTAL v.23 (Erba et al., 2022) which uses Gaussian-function basis sets. For Nd, 4f in core pseudopotentials and basis sets optimized for Nd^{2+} and Nd^{3+} species from the Stuttgart/Cologne group were used (see Supplement) with a $4s^2 4p^6 3d^1$ valence configuration (Dolg et al., 1993; Yang and Dolg, 2005). To test the reliability of 4f in core pseudopotentials, a test calculation of Nd_2O_3 was performed using a pob-TZVP 4f in valence basis set for Nd and spin-polarization with Nd in ferromagnetic configuration. Magnetic moments were locked for the first 30 self-consistent field (SCF) cycles and were then free to relax. Using a 4f in core pseudopotential has previously been shown to produce high-quality results for isotope fractionation in Ce and Eu compounds by overcoming convergence issues and saving computation time (Schauble, 2023; Schauble, 2024). For all other elements, the pob-TZVP basis set was used which is an Ahlrichs def2 basis set optimized for solid systems (Vilela Oliveira et al., 2019). Due to the large number of atoms in supercells required for phonon calculations using the finite displacement method in CRYSTAL, reduced partition function ratios for minerals were approximated by the force constant (Bigeleisen, 1955; Bigeleisen and Mayer, 1947):

$$\beta_{MD} \approx 1 + \frac{h^2}{96\pi^2 k_B^2 T^2} \left(\frac{m^{146}Nd - m^{144}Nd}{m^{146}Nd \times m^{144}Nd} \right) \Sigma F \quad (5)$$

where h is Planck's constant, k_B is Boltzmann's constant, T is the absolute temperature, m is the mass of Nd isotopes, and ΣF is the sum of the force constants in three orthogonal directions acting on a Nd atom. This approach is valid if vibrational frequencies $\omega < 1.39 \times T$ [K]. While $10^3 \ln\beta$ is particularly sensitive to high vibrational frequencies (>600 cm^{-1}), the contribution of Nd above such frequencies is very minor, and frequencies are rarely >1000 cm^{-1}. This makes the β-factors calculated here applicable to systems with T > 300 °C. As this study is concerned with isotope fractionation of Nd in medium to high-temperature systems, using the force constant approximation should provide reliable insights into the isotope fractionation. Atomic positions and cell constants were optimized until the average force on atoms was $<3.0 \times 10^{-5}$ E_h/a_0, the average atomic movement between two optimization steps was $<1.2 \times 10^{-4}$ a_0, and the energy change between two optimization steps was $<1.0 \times 10^{-9}$ E_h. Convergence criterium for the total energy was 1.0×10^{-9} E_h. E_h and a_0 correspond to Hartree energy and Bohr radius, respectively. A shrinking factor of 8 was sufficient to converge energy differences to $< 1.0 \times 10^{-9}$ E_h. The B3LYP hybrid functional based on Becke's exchange–correlation functional (Becke, 1993) with

non-local correlation by Lee et al. (1988) was used. The force constant is calculated from the change in total energy by displacing a Nd atom from its relaxed position in steps of ±0.0125 and ±0.025 Å or ±0.010 and ±0.020 Å. The force constant was determined numerically by fitting the total energies and corresponding displacements to a polynomial (Moynier et al., 2011; Nie et al., 2021; Schauble, 2011):

$$E_{tot} = \frac{1}{2}Fx^2 + c \quad (6)$$

where x is the displacement and c is the vertical intercept. Eq. (6) implies that atoms behave as a harmonic oscillator in small distances from their equilibrium position. For NdO, and Nd_2O_3, the unit cell was expanded to a 2 × 2 × 2 supercell to keep significant distance (>5 Å) between periodic images of the displaced Nd atom. For oldhamite a 2 × 2 × 2 supercell was also required to obtain a meaningful β-factor. First approximations of the geometries of the minerals were taken from the American Mineralogist Database (Downs and Hall-Wallace, 2003), the Materials Project Database (Jain et al., 2013), and the Crystallography Open Database (Gražulis et al., 2009). For allanite, a spin-polarized calculation was performed with a ferromagnetic spin configuration with the two Fe^{2+} atoms having an up spin.

As lanthanides occur often as substitutes for other metal cations in minerals, unit cells of those minerals were doped with Nd partitioning into the M-site and other anions like Al, or P into the tetrahedral site for charge balance (Table S1). The doped minerals include the accessory phases fluorapatite, zircon, titanite, xenotime, perovskite, and oldhamite as well as the main rock forming endmember minerals diopside, enstatite, forsterite, and anorthite. In fluorapatite, Nd can substitute into two different Ca sites. Calcium is either bound to 9 oxygen or 6 oxygen and one fluorine. In general, REE^{3+} substitute Ca^{2+} in apatite and Nd prefers the 7-fold site. The unit cell is charge balanced by replacing another Ca^{2+} with Na^{+} (Pan and Fleet, 2002). In zircon, Nd^{3+} substitutes Zr^{4+} and the unit cell charge is balanced by substituting Si^{4+} with P^{5+} (Finch et al., 2001; Hanchar et al., 2001). In titanite, Ti^{4+} substitution by Al^{3+} is common, which is balanced by Nd^{3+} substitution in the Ca^{2+} site (Seifert, 2005). In Perovskite, Nd^{3+} also substitutes Ca^{2+} (Goethals et al., 2019). In diopside and anorthite, Nd^{3+} substitutes Ca^{2+} and Si^{4+} is substituted by Al^{3+} (Bindeman and Davis, 2000; Schoneveld and O'Neill, 2019; Schosnig and Hoffer, 1998). Although the substitution of Ca^{2+} by Na^{+} is also common in anorthite to achieve charge balance (Dohmen and Blundy, 2014; Sun et al., 2017), it was not modelled here. Similarly, in enstatite and forsterite, Nd^{3+} replaces Mg^{2+} and Al^{3+} substitutes Si^{4+} (Burnham and O'Neill, 2020).

To validate the force constant approximation, the $10^3\ln\beta_{MD}$ of Nd_2O_3 was calculated from the phonon frequencies in the harmonic approximation of the independent modes of Nd_2O_3 after Bigeleisen and Mayer (1947):

$$\beta_{MD} = \left[\prod_{i=1}^{3N} \frac{u_i}{u'_i} \frac{\exp(-u_i/2)}{\exp(-u'_i/2)} \frac{1-\exp(-u'_i)}{1-\exp(-u_i)}\right]^{1/n} \quad (7)$$

using

$$u_i = ch\omega_i/k_BT \quad (8)$$

where N is the number of atoms in the unit cell, n is the number of substituted Nd atoms in the supercell, c is the speed of light, and ω are the vibrational frequencies. The primed species is the isotopically lighter one. For molecules, the number of vibrational frequencies is 3 N−6, while for linear molecules it is only 3 N−5. The vibrational modes were calculated using the finite displacement method at the Γ-point and additional 7 q-points in the Brillouin zone of a 2 × 2 × 2 supercell, and 26 q-points in a 3 × 3 × 3 supercell (Table 1). Sampling 27 q-points in a 3 × 3 × 3 supercell for Nd_2O_3 changed the $10^3\ln\beta$ value only by 0.006 ‰ at 25 °C (Table 1) which demonstrates convergence of $10^3\ln\beta$. Using a 3 × 3 × 3 supercell or larger for all other minerals was computationally not feasible because of the large number of atoms in the supercell. Especially for doped minerals which lose their symmetry due to the doping which makes computational efforts even more expensive.

Table 1
Reduced partition function ratios ($10^3\ln\beta_{MD}$) for Nd_2O_3 derived from phonon dispersion and the force constant approximation.

Method	Supercell	$10^3\ln\beta_{MD}$
Phonon dispersion	3 × 3 × 3	0.934
Phonon dispersion	2 × 2 × 2	0.928
Force constant	2 × 2 × 2	0.952
Force constant	1 × 1 × 1	0.680

2.2. Nuclear field shift

Calculations of the NFS effect followed the methodology described in Schauble (2013) which combines relativistic Dirac-Hartree-Fock calculations with Density Functional Theory with Projector Augmented Waves (DFT-PAW). Minerals are modelled with periodic boundary conditions and calculated Fermi contact densities $|\Psi(0)|^2$ are converted to energy shifts using a calibration set of simple molecules (NdF_3, NdF_4^-, $NdCl_4^-$, $Nd(OH)_4$; Fig. 1, Table S2). Using ions (Nd^{2+}, Nd^{3+}, Nd^{4+}) did not result in a meaningful calibration curve (see *4.1.2*). This behaviour has also been observed for Ce (Schauble, 2024). The reason why relativistic all-electron calculations and DFT-PAW do not agree for ions and molecules of lanthanides is unclear at present, although it might be related to a shortcoming of the codes. Total energies of the calibration set molecules were calculated with relativistic all-electron calculations using the Dirac-Hartree-Fock method in Dirac v.21 (Saue et al., 2020) with the exact two component Hamiltonian (X2C). For Nd, an all-electron double zeta Dyall basis set (ae2z) (Gomes et al., 2010) was used and a def2-SVP basis set (Weigend and Ahlrichs, 2005) was used for all other elements. A relativistic basis set is required for Nd as it is a heavy element (Z > 40) which makes relativistic effects significant. Given relativistic effects are negligible in lighter elements (e.g. H, O, F, Cl), the non-relativistic def2-SVP basis set was used. The gaussian exponent ξ was calculated from the nuclear charge radius $<r^2>$ taken from Angeli and Marinova (2013) using (Visscher and Dyall, 1997):

$$\xi = \frac{3}{2\times < r^2 >} \quad (9)$$

Fermi contact densities were calculated in ABINIT v.10.2.4.8 (Gonze

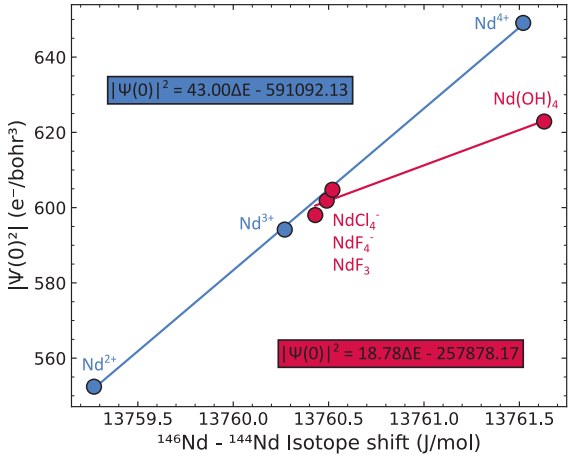

Fig. 1. Calibration set of Nd^{3+} and Nd^{4+} molecules. Energy shifts are derived from relativistic all-electron calculations in a finite cluster and plotted against fermi contact densities calculated with DFT-PAW with periodic boundaries. The solid line represents the linear regression line.

et al., 2020) using the PBE functional (Perdew et al., 1996). The PAW datasets for Ce, and Nd were taken from the lanthanide library of Topsakal and Wentzcovitch (2014). Datasets for all other elements were from the JTH library (Jollet et al., 2014). The fermi contact density $|\Psi(0)|^2$ was then calculated on the B3LYP-optimized geometries from the mass-dependent calculations without another relaxation step at the DFT–PAW level. Geometry optimizations have been found not to affect the fermi contact density significantly (Schauble, 2013). Molecules were modelled in a 10 × 10 × 10 Å box to minimize interaction between periodic images. An energy cut off of 40 E_h and a fine grid cut off of 100 E_h was used. Total energies were converged to a change between two electron minimization steps of $<1.0 \times 10^{-7}$ E_h using Pulay mixing. Using a lower threshold did not significantly change the electron density. A Hubbard U value of 2.5 and 3.1 eV was applied to the f-orbital of Ce and Nd, respectively. The values are recommended by the designer of the PAW-datasets (Topsakal and Wentzcovitch, 2014). The NFS effect between two Nd species A and B was then calculated after Bigeleisen (1996):

$$10^3 ln\alpha_{NFS} = \frac{(E[^{146}NdB] - E[^{144}NdB]) - (E[^{146}NdA] - E[^{144}NdA])}{N_A k_B T} \quad (10)$$

where E is the total energy, and N_A is Avogadro's constant. The NFS is reported as α-notation relative to Nd_2O_3 instead of a Nd-vapour because the Fermi contact density of a Nd-vapour cannot readily be calculated. In order to make the two isotope fractionation effects comparable, the mass-dependent effect is also reported relative to Nd_2O_3.

3. Results

The modelled Nd-species are visualized in Fig. 2. Table 2 presents the sum of the force constants ΣF and fermi contact densities $|\Psi(0)|^2$ that were used to calculate reduced partition function ratios. The polynomial coefficients A1, A2, and B are given in Table S3, in order to calculate $10^3\ln\alpha_{TOT}$ for a specific temperature using the equation:

$$10^3 ln\alpha_{TOT} = \frac{A1}{T^2} + \frac{A2}{T^4} + \frac{B}{T} \quad (11)$$

The term $A1/T^2 + A2/T^4$ represents the mass-dependent fractionation which is nearly proportional to $1/T^2$, while B/T represents the NFS. The two isotope fractionation effects were fitted separately. As shown in Fig. 3a, for most species the mass-dependent component is nearly proportional to $1/T^2$, except for the NdO molecule which shows a more concave trend. Concave trends are common in species where the element of interest is directly bound to hydrogen or low mass molecules (Schauble, 2004). The mass dependent fractionation of the Nd–species is separated by their oxidation state with Nd^{2+} species being isotopically lighter than Nd^{3+} species. Overall, $10^3\ln\alpha_{MD}$ values range from −0.498 ‰ for Nd^{2+} monoxide crystal to 0.700 ‰ for Nd^{3+} in zircon at 25 °C. Accordingly, sum of the force constants ΣF are higher in Nd^{3+} species and range from 349 to 1053 N/m whereas NdO has a ΣF of only 289 N/m. In oldhamite Nd^{3+} has a drastically different bonding environment given it is bound to S which resulted in a significantly lower force constant of 349 N/m (Fig. 3b).

In contrast, calculated NFS values are proportional to 1/T (Fig. 3c). The magnitude of fractionation between Nd^{3+} species is much smaller for the NFS compared to the mass-dependent component. For example, $10^3\ln\alpha_{NFS}$ in Nd^{3+} species ranges only from −0.053 ‰ to 0.244 ‰ (Δ = 0.298), compared to a range of −0.053 ‰ to 0.700 ‰ (Δ = 1.104) for mass-dependent $10^3\ln\alpha_{MD}$ at 25 °C. Nd^0-metal is isotopically the lightest, but Nd^{2+} species are heavier than Nd^{3+} species by approximately 0.423 ‰ at 25 °C. This is reflected in the lower electron density at the nucleus $|\Psi(0)|^2$ in Nd^{2+} species (~580 $e^-/bohr^3$) opposed to Nd^{3+} species (~601 $e^-/bohr^3$) and Nd^0-metal (~611 $e^-/bohr^3$). Species were Nd^{3+} substitutes Ce^{3+} have slightly lower electron densities (590 $e^-/bohr^3$).

Nd-O bond lengths range from 2.31 to 2.73 Å in Nd^{3+} species, while molecular NdO and solid NdO have a Nd-O length of 1.77 and 2.49 Å, respectively (Table 2). Coordination numbers (CN) range from 7 to 11 in Nd^{3+} species and mostly represent the number of direct oxygen neighbour atoms, although Nd in fluorapatite and bastnäsite is also bound to fluorine (see Fig. 2). In solid NdO, Nd has a CN of only 6. The mass-dependent fractionation also displays a moderate correlation with Nd-O bonds in Nd^{3+} species ($r^2 = 0.72$; Fig. 4a). The correlation with coordination number is much weaker and not significant ($r^2 = 0.25$; Fig. 4b). Isotope fractionation also appears to be related to the substituted cation (Fig. 4c). Minerals like forsterite and enstatite where Nd^{3+} substitutes Mg^{2+} are isotopically heavier than minerals where Ca^{2+} is the substituted cation. While minerals such as allanite and monazite which host light REE and Th as their main cations are isotopically the lightest.

4. Discussion

4.1. Validation of ab initio calculations

4.1.1. Validation of mass-dependent fractionation factors

In order to validate the force constant approximation, we also calculated the reduced partition function ratio ($10^3\ln\beta_{MD}$) for crystalline Nd_2O_3 from vibrational frequencies (Eq. (7)) and compared derived frequencies at the Γ-point with experimental data (Table 3). The vibrational spectrum of Nd_2O_3 derived from DFT calculations does not change significantly between the PBE, PBE0, and B3LYP functionals. B3LYP overestimates vibrational frequencies by 2.75 % on average relative to experimental data whereas PBE by only 1.32 % on average (Table 3). Treating 4f electrons explicitly also resulted in a deviation from experimental frequencies by only 1.41 % on average. Unfortunately, uncertainties on the experimental vibrational frequencies are not given. The $10^3\ln\beta_{MD}$ value for Nd_2O_3 approximated using the sum of the force constants (Eq. (5); 0.952 at 25 °C) using B3LYP is therefore slightly overestimated by 0.024. As shown in Fig. 5, however, any overestimation becomes negligible at temperatures >300 °C which makes the force constant approximation applicable to the high temperature systems discussed here. The PBESOL0 hybrid functional clearly overestimates vibrational frequencies by 8.43 % on average but the obtained lattice constants are in excellent agreement with experimental data because PBESOL0 is particularly optimized for lattice constants but no other parameters (Table 3). The PBESOL0 functional represents the PBESOL functional mixed with 25 % Hartree-Fock exchange. Similarly, the PBE0 hybrid functional overestimates vibrational frequencies by 5.46 % on average.

Comparing the Nd^{3+} species reported here with previous calculations of Ce^{3+} species (Schauble, 2024), we see that the isotope fractionation factors show similar trends and are strongly correlated ($r^2 = 0.97$; Fig. 6). Minerals like monazite and bastnäsite are isotopically light, minerals like apatite and diopside where REE^{3+} substitutes Ca^{2+} are slightly heavier by ~0.1–0.3 ‰ relative to monazite (at 25 °C), while REE^{3+} in zircon is exceptionally heavy (~0.82–0.85 ‰ relative to monazite). Given Nd and Ce are close neighbours on the periodic table, this similar behaviour is in line with expectations.

Studies by Ma et al. (2024) and Chen et al. (2020) compared doped unit cells with larger supercells for the $^{60}Ni/^{58}Ni$ and $^{94}Zr/^{90}Zr$ ratios, respectively, which are potentially a more realistic representation. However, this approach increases the demand for supercomputer time enormously, with a limit difference in the results with these studies showing that increasing the unit cell can change the force constant by up to 4 N/m. Here, substitution-tests on Ce endmembers Ce-monazite (1/4 Nd) and Ce-bastnäsite (1/3 Nd) show differences in ΣF of 6 and 3 N/m, respectively compared to pure Nd monazite and Nd-bastnäsite. A difference of 6 N/m drives a difference in $10^3\ln\beta_{MD}$ of 0.009 ‰ at 25 °C and 0.002 ‰ at 300 °C for the $^{146}Nd/^{144}Nd$ ratio which is significantly below achievable analytical uncertainties (±0.015 ‰). Running further tests

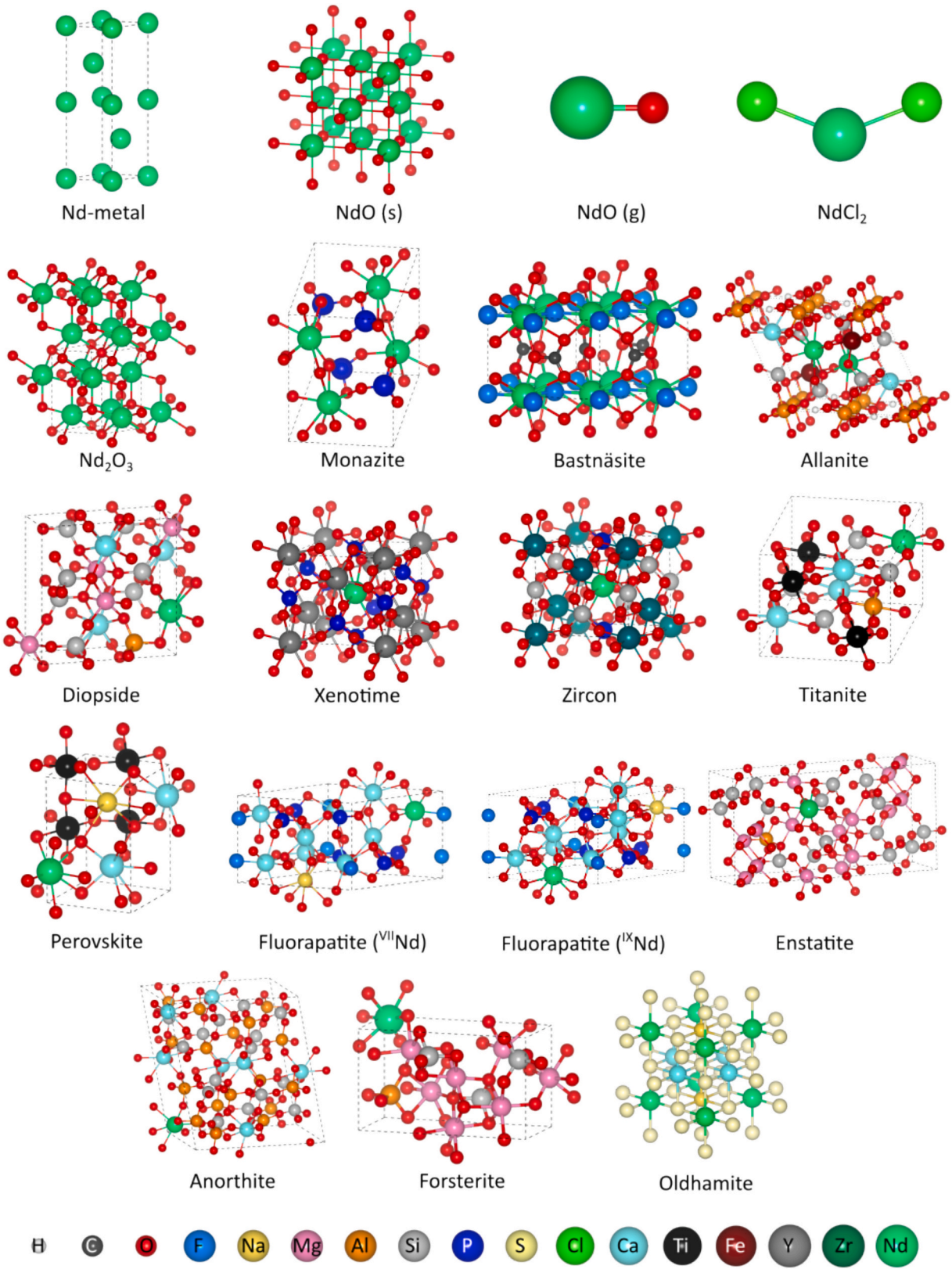

Fig. 2. Overview of modelled Nd species in this study. Species include Nd^0, Nd^{2+}, and Nd^{3+} species. Modelled species include accessory minerals, major rock forming minerals, and gaseous species.

Table 2
Modelled Nd species are given with the calculated sum of the force constants ΣF, the average Nd-O bond length in the species, the coordination number (CN) of Nd in the unit cell, and the electron density at the nucleus of Nd $|\Psi(0)|^2$. Substitution of cations was done after Table S1.

Species	Formula	ΣF (N/m)	Nd-O (Å)	CN	$\|\Psi(0)\|^2$ (e-/bohr^3)
Nd^0 species					
Nd-metal	Nd^0	–	–	8	611.37
Nd^{2+} species					
Nd monoxide (s)	NdO	289	2.49	6	587.96
Nd monoxide (g)	NdO	–	1.95	–	580.55
Nd dichloride (g)	$NdCl_2$	–	–	–	577.42
Nd^{3+} species					
Nd_2O_3 (hexagonal)	Nd_2O_3	607	2.51	8	603.06
Nd-Monazite	$NdPO_4$	499	2.58	9	599.92
Ce-Monazite	$Ce_{0.75}Nd_{0.25}PO_4$	493	2.60		591.69
Nd-Bastnäsite	$NdCO_3F$	457	2.69	11	599.38
Ce-Bastnäsite	$Ce_{0.67}Nd_{0.33}CO_3F$	454	2.73		591.91
Allanite	$CaNd(Al_2Fe)Si_2O_7[SiO_4]O(OH)$	492	2.60	8	–
Diopside	$MgCa_{0.75}Nd_{0.25}Si_{1.75}Al_{0.25}O_6$	683	2.55	8	601.33
Xenotime	$Y_{0.75}Nd_{0.25}PO_4$	859	2.43	8	602.49
Zircon	$Zr_{0.75}Nd_{0.25}Si_{0.75}P_{0.25}O_4$	1053	2.37	8	605.55
Titanite	$Ca_{0.75}Nd_{0.25}Ti_{0.75}Al_{0.25}SiO_5$	623	2.49	7	600.73
Perovskite	$Nd_{0.33}Na_{0.33}Ca_{0.33}TiO_3$	616	2.52	8	601.78
Fluorapatite (^{VII}Nd)	$Ca_4Nd_{0.5}Na_{0.5}(PO_4)_3F$	578	2.50	7	601.14
Fluorapatite (^{IX}Nd)	$Ca_4Nd_{0.5}Na_{0.5}(PO_4)_3F$	688	2.55	9	600.71
Enstatite	$Nd_{0.0625}Mg_{0.9375}Al_{0.0625}Si_{0.9375}O_3$	841	2.37	6	604.79
Anorthite	$Nd_{0.125}Ca_{0.875}Si_{1.875}Al_{2.125}O_8$	576	2.53	7	–
Forsterite	$Nd_{0.25}Mg_{1.75}Al_{0.25}Si_{0.75}O_4$	798	2.31	6	603.27
Oldhamite	$Nd_{0.25}Na_{0.25}Ca_{0.5}S$	349	–	6	599.94

VII and IX correspond to 7- and 9-fold coordination, respectively.

with larger supercells would be computationally expensive and is unlikely to significantly alter the results presented here. Given the focus of this study is high-temperature systems (>300 °C), we conclude that minor variations in force constants due to potential concentration dilution effects are not significant. However, we acknowledge previous efforts on quantifying concentration effects for other elements (Duan and Huang, 2024; Feng et al., 2014; Ma et al., 2024) which remains a worthy objective for future studies of the lanthanides.

4.1.2. Validation of the nuclear field shift effect

Nd^{2+} species have a lower electron density at the nucleus (i.e. $|\Psi(0)|^2$) compared to a Nd^0–metal due to the loss of two s-electrons. By increasing the oxidation state from 2+ to 3+ an f–electron is removed. The reduced shielding from the loss of an f–electron increases the attraction of the nucleus on all the remaining electrons, moving them closer to the nucleus which results in an increase in $|\Psi(0)|^2$ from Nd^{2+} to Nd^{3+}. As isotopes with a larger volume, which in this instance is ^{146}Nd, prefer bonding environments with a lower electron density at the nucleus, the Nd^{2+} species are isotopically heavier than Nd^{3+} species. The NFS between Nd^{3+} species does not dominate the total isotope fractionation observed and reaches a maximum of 0.298 ‰ at 25 °C (Fig. 3c) because electron density does not change considerably without adding or removing electrons. This is in stark contrast to the mass-dependent fractionation which reaches a maximum of 1.194 ‰ among Nd^{3+} species at 25 °C (Fig. 3a).

Mössbauer isomer shifts scale with the difference in electron density at the nucleus and are related to the NFS effect. Studies of isomer shifts in Nd are scarce but a study by Kaindl (1970) provides a comprehensive overview of isomer shifts between Nd^0, Nd^{2+} and Nd^{3+} compounds for the 75.5 keV transition in ^{145}Nd. The change in $<r^2>$ for the 75.5 keV transition in ^{145}Nd reported in Kaindl (1970) is 0.0019 ± 0.0009 fm^2. Unfortunately, the large uncertainty (47.4 %) for $\delta<r^2>$ leaves a large range of possible isotope fractionation. Assuming differences in electron density between Nd compounds are very similar to those between Sm compounds (Knyazev and Myasoedov, 2001), we also reviewed isomer shifts in Sm compounds for the 22.5 keV transition in ^{149}Sm. The change in nuclear charge radius between the excited and ground state of ^{149}Sm was reported by Eibschütz et al. (1972) as 0.0012 ± 0.0001 fm^2 which considerably reduces the analytical uncertainties (8.3 %) on the experimental values. Table 4 represents the isotope fractionation between metallic Nd^0, $NdCl_2$, and Nd_2O_3 species derived from *ab initio* calculations. The values are compared with experimental data from Kaindl (1970) for Nd and Coey et al. (1976) for Sm compounds. Eibschütz et al. (1972) presented their Sm isomer shifts only graphically (not numerically) making them unusable. The experimental isomer shifts (δ) in mm/s are converted into energy shifts using:

$$\Delta E = \delta \times \frac{h\nu_\gamma}{c} \tag{12}$$

and scaled to ^{146}Nd/^{144}Nd using:

$$\Delta E_{146/144Nd} = \Delta E_{145^*/145Nd} \times \frac{< r^2_{146Nd} > - < r^2_{144Nd} >}{< r^2_{145Nd^*} > - < r^2_{145Nd} >} \tag{13}$$

where $h\nu_\gamma$ is the energy difference between the excited and ground state. Note that Sm_2O_3 reported in Coey et al. (1976) represents a monoclinic C-Type phase different than the hexagonal Nd_2O_3 A-Type phase here. Also, isomer shifts are measured in solid $NdCl_2$ and $SmCl_2$ halides and not molecules. However, we see that the isotope fractionation between Nd species, computed in this study, are in good agreement with experimental data derived from Nd and Sm compounds (Table 4).

4.1.3. Effect of isotope pair on nuclear field shift effect

Minimizing the NFS effect among Nd^{3+} species requires the use of the ratio which has the lowest difference in nuclear charge radii ($\delta<r^2>$; Table S4; Angeli and Marinova (2013), Fricke et al. (2004)). This would be ^{146}Nd/^{145}Nd, however, using this ratio would be at the expense of the magnitude of the mass-dependent effect because of the smaller relative mass difference between ^{146}Nd and ^{145}Nd (1.001 amu) opposed to ^{146}Nd/^{144}Nd (2.003 amu), as mass-dependent fractionation scales with Δm (Urey, 1947). The ^{146}Nd/^{144}Nd ratio has the second lowest $\delta<r^2>$ and is therefore a good compromise by maintaining a small NFS effect while still having a 2 amu mass difference (Table S4). The change in $<r^2>$ between Nd isotope ratios can reach up to 1.282 fm^2 which is ~4.66 times higher than for the ^{146}Nd/^{144}Nd ratio utilised in this study. This might be useful where a high fractionation magnitude is desirable. For example, for understanding the fractionation between Nd^{2+} and Nd^{3+} at high temperatures under solar nebula conditions. The smallest

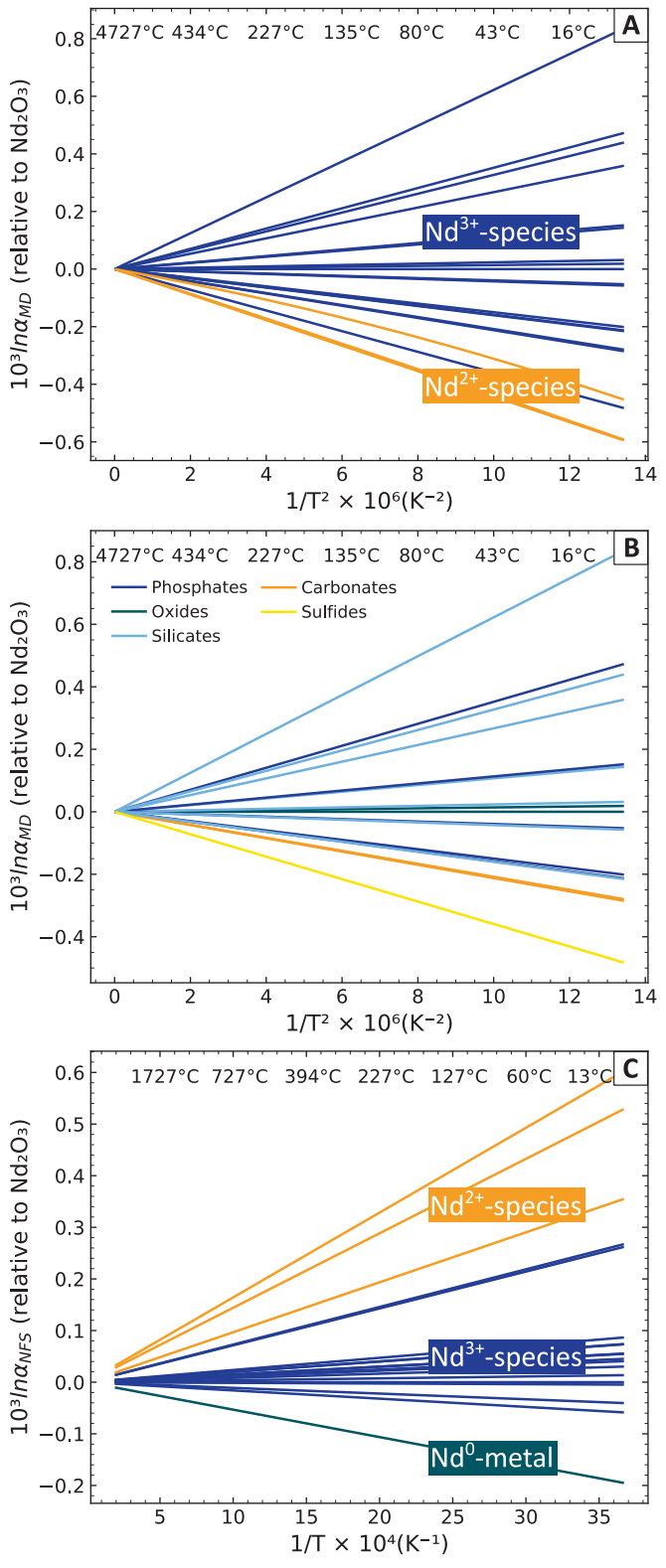

Fig. 3. (A) Mass-dependent isotope fractionation as $10^3\ln\alpha_{MD}$ relative to Nd_2O_3 is nearly proportional to $1/T^2$. Higher oxidation states are isotopically heavier. (B) Isotope fractionation factors for Nd^{3+} species. The sulfide phase oldhamite is isotopically lighter than silicates (allanite, diopside, titanite, anorthite, enstatite, forsterite, zircon), oxides (Nd_2O_3, perovskite), carbonates (bastnäsite), and phosphates (monazite, apatite, xenotime). (C) Nuclear field shift fractionation as $10^3\ln\alpha_{NFS}$ relative to Nd_2O_3 shows a proportionality to $1/T$. The isotope with the larger volume, ^{146}Nd in this instance, is preferentially incorporated into species with the lower electron density at the nucleus which follows $Nd^{2+} < Nd^{3+} < Nd^0$.

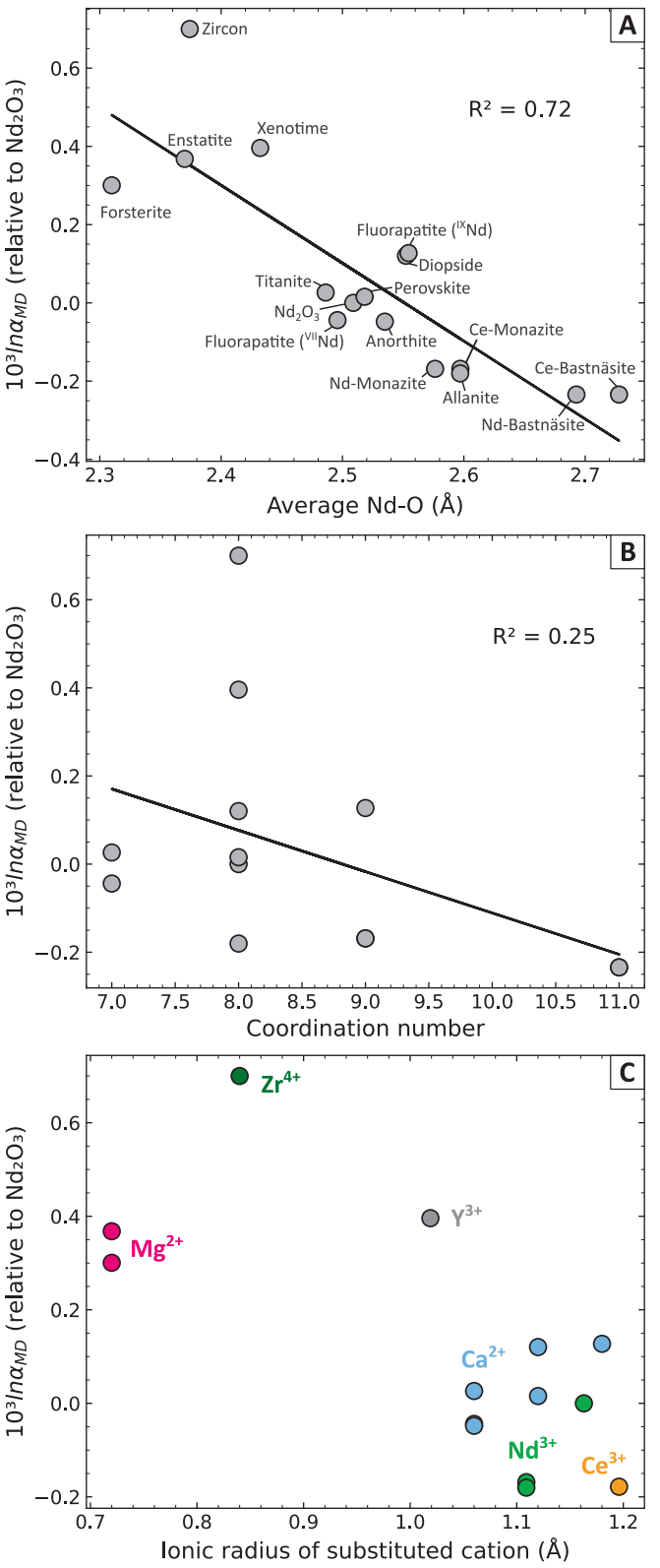

Fig. 4. (A) Mass-dependent isotope fractionation factors $10^3\ln\alpha_{MD}$ are moderately correlated with the average Nd-O bond length ($r^2 = 0.72$). (B) The isotope fractionation factor is not significantly correlated with the coordination number (CN) of Nd ($r^2 = 0.25$). (C) Isotope fractionation by substitution into crystal lattices is strongly dependent on the ionic radius of the substituted cation. Phases in which Mg^{2+}, Zr^{4+}, and Y^{3+} is substituted appear to be isotopically heavier than phases where Ca^{2+} is substituted or Ce^{3+} and Nd^{3+} phases like monazite and bastnäsite. Data for the ionic radii are from Shannon (1976).

Table 3
Experimental lattice parameters and vibrational frequencies of Nd_2O_3 are compared with ab initio calculations using the exchange correlation functionals PBE, PBESOL0, PBE0 and B3LYP. Deviations in % from experimental data are given in extra columns.

	PBE		PBESOL0		PBE0		B3LYP		B3LYP		Experimental
4f treatment	in core		in core		in core		in core		in valence		
*Lattice parameters (Å)**		*Deviation (%)*		*Deviation (%)*		*Deviation (%)*		*Deviation (%)*		*Deviation (%)*	
a	3.8974	1.70	3.8521	0.54	3.8717	1.05	3.9006	1.78	3.8291	0.06	3.8312 ± 0.0001
c	6.1294	2.08	5.9849	0.28	6.0744	1.20	6.1854	2.97	6.0817	1.31	6.0017 ± 0.0003
Vibrational frequencies at Γ-point (cm^{-1})†											
Eg	104.8	0.70	116.4	9.36	110.50	4.52	106.4	0.86	105.9	0.36	105.5
A1g	196.0	2.19	213.1	10.05	201.38	4.81	198.2	3.29	191.0	0.37	191.7
A1g	425.9	0.19	452.0	5.60	450.33	5.25	439.5	2.91	436.3	2.21	426.7
Eg	444.9	2.19	476.5	8.69	469.23	7.27	453.1	3.96	423.6	2.71	435.1
$10^3 \ln\beta_{MD}$ (25 °C)	0.920		1.079		1.004		0.928		0.934		

*Experimental lattice parameters from Umesh et al. (2011).
†Experimental vibrational frequencies from Yadav et al. (2021).

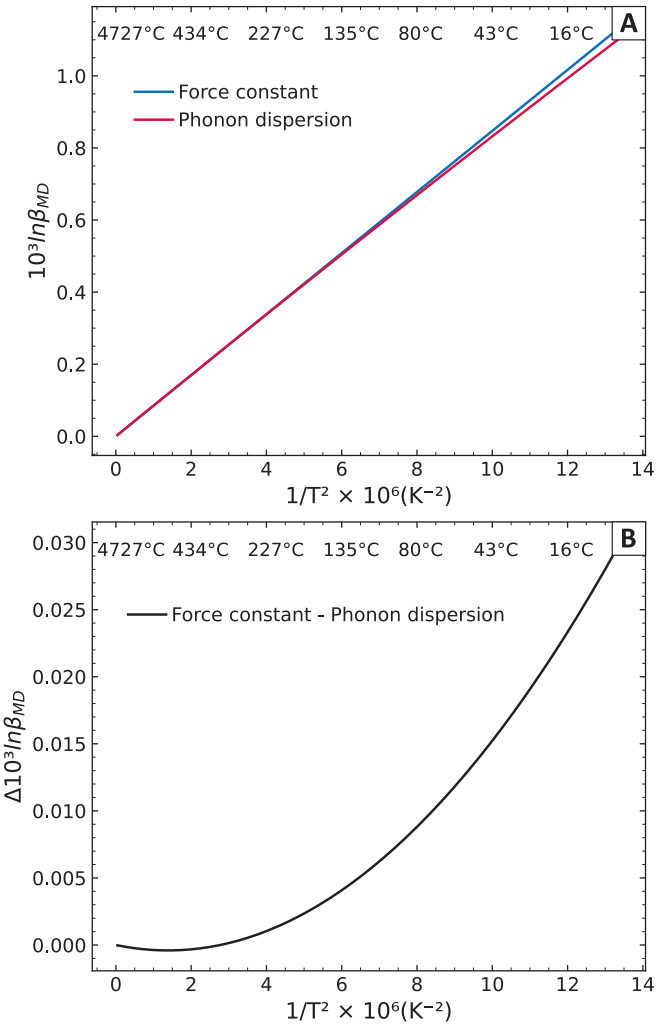

Fig. 5. (A) Difference between $10^3 \ln\beta$ for Nd_2O_3 calculated using the force constant approximation and phonon frequencies. (B) The difference between both methods becomes negligible at temperature >300 °C which makes the force constant approximation applicable to high temperature systems.

difference in nuclear charge radius between two different stable Nd isotopes is 0.161–0.169 fm^2 (Table S4). This does not allow the (near) elimination of the NFS effect by choosing a suitable isotope pair like for Ce where ^{136}Ce, ^{138}Ce, and ^{140}Ce have very similar $<r^2>$ (see Fig. 7b in Nestmeyer and McCoy-West (2025)).

4.2. Earth's differentiation

4.2.1. Implications for crust-mantle differentiation

Most igneous rocks display $\delta^{146}Nd$ compositions close to chondritic compositions (−0.027 ± 0.005 ‰ 95 % ci; McCoy-West et al. (2017); Fig. 7). Mid-ocean ridge basalts (MORB), ocean-island basalt (OIB), and island-arc basalt (IAB) have mean compositions of −0.025 ± 0.003 ‰, −0.033 ± 0.004 ‰, and −0.018 ± 0.0011 ‰, respectively; (Bai et al. (2022), McCoy-West et al. (2017), McCoy-West et al. (2021); Table S5). Therefore, McCoy-West et al. (2021) estimated the BSE to have a $\delta^{146}Nd$ composition of −0.024 ± 0.003 ‰. This similarity suggests minimal isotope fractionation during mantle melting assuming the bulk silicate Earth (BSE) has a chondritic composition.

The force constant of Nd^{3+} in silicate melt cannot be easily calculated in order to quantify the isotope fractionation between parental rocks and melts. There is experimental data on the bonding environment of Nd^{3+} in silicate glass which is often used as an approximation for melts (Sen,

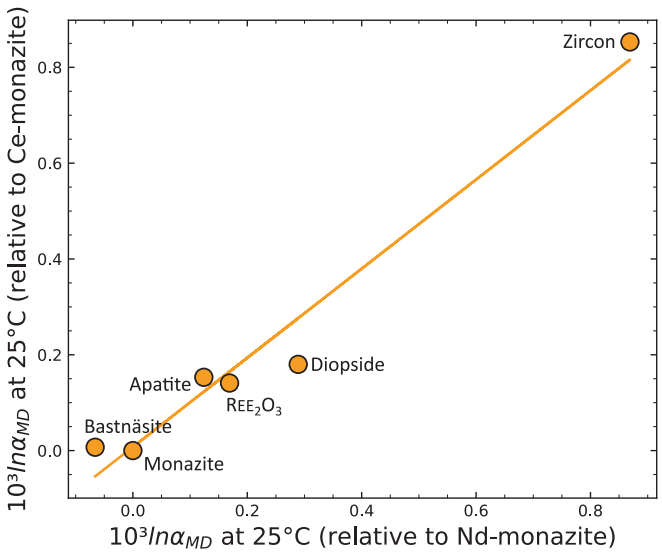

Fig. 6. Isotope fractionation factor for selected Nd species relative to monazite compared with data of Ce species from Schauble (2024) (r^2 = 0.97). The fractionation factors show a linear trend indicating a similar fractionation between minerals because of Nd and Ce being close neighbours in the periodic table.

Table 4
Calculated nuclear field shift effect between Nd-metal and a Nd^{3+} and Nd^{2+} species compared with experimental data.

Compounds	$^{146/144}$Nd $10^3\ln\alpha_{NFS}$		Scaled $^{145*/145}$Nd $10^3\ln\alpha_{NFS}$	Scaled $^{149*/149}$Sm $10^3\ln\alpha_{NFS}$
	Ab initio		*Experimental*	*Experimental*
	Molecule calibration	Ion calibration		
Nd-metal → $NdCl_2$	0.73	0.32	0.39–1.30 (0.84)	0.59–0.79 (0.69)
Nd-metal → Nd_2O_3	0.18	0.08	0.06–0.32 (0.19)	0.09–0.30 (0.19)

The experimental values are derived from isomer shifts of the ^{145}Nd* and ^{149}Sm* transition, with average values in brackets. The range in experimental values comes from the uncertainty of the change in $<r^2>$ between the excited state and the ground state and uncertainties in the reported isomer shifts. Experimental data for ^{145}Nd* from Kaindl (1970) and for ^{149}Sm* from Coey et al. (1976). The $10^3\ln\alpha$ values correspond to 25 °C.

2000). However, recent molecular dynamics simulations have shown that the force constants of Ca and Fe in silicate melts are strongly dependent on the melt composition (e.g. trachyte, dacite, basalt, phonolite, basanite melt (Li et al., 2025; Rabin et al., 2023)). Additionally, these studies found a clear relationship between melt composition, force constant, and metal-oxide bond lengths. Conversely, the study by Hu et al. (2023b) focusing on lanthanides found no change in force constants for Dy^{3+} and Eu^{3+} between silicate glass of basaltic, andesitic, and rhyolitic composition which suggests that the force constant of Nd^{3+} in silicate glass could also be independent of the melt composition and Nd-O bond length in stark contrast to the molecular dynamics simulations. Sen (2000) reported Nd-O bond length of 2.35 Å and 2.62 Å for Al-free and Al-rich (Al_2O_3 = 7300 ppm) silicate glass, respectively, and proposed that doping of silicate glass with Nd causes Nd clusters that break up with the addition of Al. This homogenization of Nd in silicate glass leads to a large increase in Nd–O bond lengths along with a change of the Nd coordination from predominantly Nd-O-Nd to Nd–O–Al/Si. However, they observed identical Debye-Waller factors of 0.01 $Å^2$ for both silicate glasses which also suggests no difference in bond stiffness and isotope fractionation between the Al-free and Al-rich silicate glass. The mean force constant of Nd^{3+} in silicate glass reported by Hu et al. (2023b) is 171 N/m, which corresponds to a sum of the force constants of 513 N/m. Strictly speaking, this experimental value is not directly comparable to the calculated force constants here. However, Fe force constants derived by NRIXS and *ab initio* calculations for some Fe bearing minerals agree within 5 – 22 N/m (Nie et al., 2021). This suggests that the reduced partition function ratio for Nd^{3+} in silicate melt ought to be within the modelled silicate minerals (454–1053 N/m).

Assuming there is a strong relationship between Nd-O bond length and force constant in silicate melt, the experimental Nd-O bond lengths in silicate glass (2.35 Å – 2.62 Å; (Sen, 2000)) are in the range of bond lengths in the modelled Nd^{3+} bearing minerals here which range from 2.31 Å in forsterite to 2.73 Å in Ce–bastnäsite. The maximum isotope fractionation between Nd^{3+} minerals is between zircon and Ce–bastnäsite which is −0.017 ‰ at 1000 °C and reaches −0.022 ‰ at 1400 °C which approaches achievable analytical uncertainties (±0.015; McCoy-West et al. (2020b)). Note that in this case isotope fractionation becomes larger with increasing temperature as mass-dependent and NFS component have opposing directions. A significant isotope fractionation between mantle and melt is, therefore, unlikely but a better quantitative understanding of the force constant of Nd^{3+} in silicate melt is required to accurately answer this question.

Curiously the mean compositions of peridotites (−0.005 ± 0.022 ‰) and komatiites (−0.005 ± 0.070 ‰), are slightly heavier than MORB and chondrites (McCoy-West et al. (2017), McCoy-West et al. (2021); Fig. 7). However, the limited data currently available for peridotites (n = 7) and komatiites (n = 2) leaves a large 95 % confidence interval that makes these rock types indistinguishable from typical basalts and a larger dataset is required to demonstrate confidently that ultramafic rocks are isotopically heavier. As the isotope fractionation of Nd is related to the substituted cation (Fig. 4c), the major chemical differences between these rock types could explain a superchondritic composition of mantle rocks. Minerals in which Nd^{3+} substitutes Mg^{2+} are isotopically heavier than minerals where Nd substitutes Ca^{2+} because of the smaller ionic radius of Mg^{2+}. Fe^{2+} has an ionic radius of 0.78 Å (Shannon, 1976) in fayalite and ferrosilite, which is more similar to Mg^{2+} in enstatite and forsterite (0.72 Å) compared to Ca^{2+} in diopside (1.12 Å) or anorthite (1.06 Å). Force constants similar to Nd^{3+} substituting Mg^{2+} can therefore be expected for Nd that substitutes for Fe^{2+}. In mantle peridotites, the heavier Nd isotopes will therefore be hosted in olivine and orthopyroxene. More importantly, regardless of the peridotite-melt fractionation, the fact that Nd incorporated in clinopyroxene is isotopically lighter than Nd in orthopyroxene and olivine, has implications for isotope fractionation during mantle melting. As the bulk of Nd in mantle peridotite is hosted in clinopyroxene (Table 5) and clinopyroxene and the aluminous phase (e.g. plagioclase, spinel or garnet) are preferentially melted during mantle melting (Green and Ringwood, 1967), heavier Nd isotopes will stay in the residual peridotite because olivine and orthopyroxene are barely melted during generation of a basaltic melt. As the Nd concentration in the residuum is much lower than in the basaltic melt, the isotopic composition has the potential to move to superchondritic values potentially resolvably heavier than a chondritic composition.

The only measured komatiites to date (Fig. 7) are from Gorgona, Colombia. Although, Gorgona is anomalous amongst komatiites being the only Phanerozoic example, they were sourced from a mantle of variable previous depletion and, therefore, likely reflect the composition of the depleted mantle (Hyung et al., 2023; Révillon et al., 2000). The fact that they show a superchondritic composition, agrees with the postulation that the depleted mantle is enriched in heavier Nd isotopes due to the mobilization of lighter Nd to the crust during partial melting. There is limited data on the isotopic composition of mantle rocks for the REE in general. For Ce, again a comprehensive dataset for mantle rocks is missing with the available data suggesting unresolvable isotope fractionation between the BSE and chondrites ($\delta^{142/140}$Ce = 0.01 ± 0.30

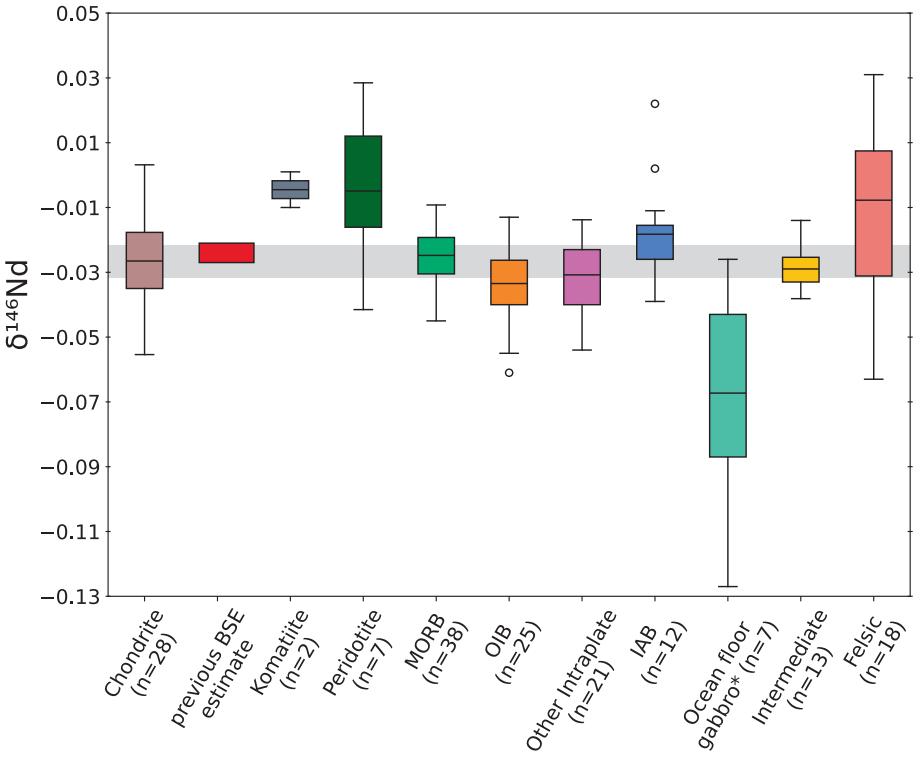

Fig. 7. Overview of stable Nd isotope data from various igneous rocks and chondrites. Peridotites and komatiites are isotopically heavier than mafic to felsic rock. Chondrites include carbonaceous, enstatite, and ordinary chondrites. Felsic rocks contain data from granites, rhyolites, and granodiorites. Intermediate rocks contain data from andesites, tonalites, diorites, and dolerites. Data compiled from Bai et al. (2021), Bai et al. (2022), McCoy-West et al. (2020b), McCoy-West et al. (2020a), McCoy-West et al. (2021), and McCoy-West et al. (2022). Coloured boxes contain 50 % of the datapoints. The remaining datapoints are within the whiskers excluding outliers which are shown as hollow circles. The line inside each box represents the mean. Abbreviations: mid-ocean-ridge basalt (MORB), ocean-island basalt (OIB), island-arc basalt (IAB), bulk silicate earth (BSE). The average chondrite composition is −0.027 ± 0.005 ‰. *Isotopic composition of gabbros is affected by diffusion processes.

Table 5
Melt-mineral partition coefficients of Nd in the main minerals of mantle peridotite (Winter, 2014).

Olivine	Opx	Cpx	Garnet
0.006	0.03	0.23	0.026

‰; Pourkhorsandi et al. (2021), Pourkhorsandi et al. (2024)). Given that, global basalts resemble chondrites, we suggest that the limited dataset of ultramafic rocks (n = 9) requires expansion to gain a better understanding of the δ^{146}Nd of the mantle relative to chondrites.

4.2.2. *Metal-sulfide-silicate differentiation*

Fractionation of stable Nd between the Earth's core and BSE has been discussed previously (McCoy-West et al., 2021; McCoy-West et al., 2017) because a reservoir of light Nd in the Earth's core could potentially explain the excess of ^{142}Nd in terrestrial samples compared to chondrites (Boyet and Carlson, 2005). Given that the Nd isotope composition of chondrites is similar to the Earth's basaltic crust (ca. 0.027 ‰; Fig. 8), a reservoir of lighter Nd isotopes in the Earth's core would be a potential explanation for the mantle being isotopically heavier than the bulk Earth. A plausible host phase that can accommodate REE is sulfur of which the outer core contains ca. 1.8–2.5 % (Allegre et al., 1995; Litasov and Shatskiy, 2016; McDonough, 2003; Wohlers and Wood, 2017). However, a S-phase in the core that can host significant amounts of REE has been questioned from an experimental perspective (Bouhifd et al., 2015). A known S-host mineral for REE in enstatite chondrites is oldhamite (CaS; Crozaz and Lundberg (1995)). The origin of oldhamite is best explained by condensation (Lodders, 1996) but also igneous processes have been proposed (Dickinson and

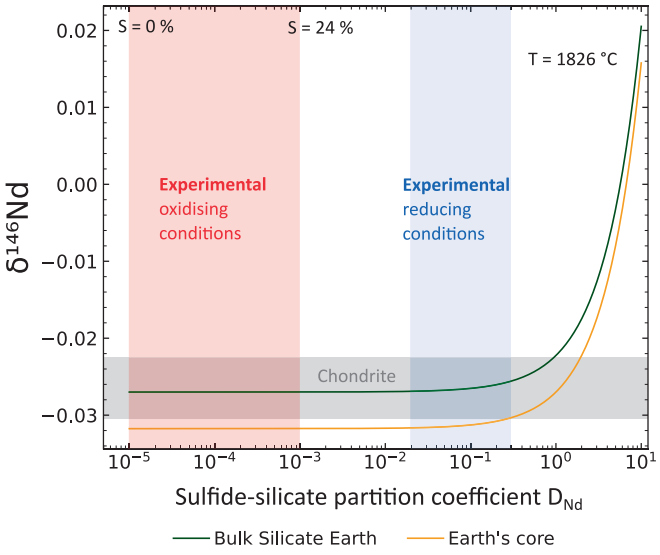

Fig. 8. Modelled equilibrium partitioning of Nd between the Earth's core and the bulk silicate Earth (BSE) at 2100 K (1826.85 °C). The highlighted areas represent experimental core-silicate partition coefficients for Nd depending on S content of the core and oxidation state of the mantle (Bouhifd et al., 2015; Wohlers and Wood, 2017). Reduced partition function ratios for Nd in monazite and oldhamite have been used for the BSE and the core, respectively, since the bulk of Nd in the core will be hosted in the sulfide phase. Based on the experimental partition coefficients of Nd, the BSE can be expected to have the same composition as the bulk Earth which is assumed to be chondritic here (δ^{146}Nd = –0.027 ‰).

McCoy, 1997). Sulfides in the Earth's core probably formed from magmatic differentiation and are not relicts of condensation. Either way, because of the vastly different bonding environment of Nd in oldhamite (i.e. to S (Nd–S) rather than O (Nd–O); Fig. 2), oldhamite provides a good approximation of the magnitude of isotope fractionation that can be expected between Nd in sulfides and silicates. The lower force constant for Nd in oldhamite derived herein (349 N/m; Table 2; Fig. 3b) suggests that a sulfide phase segregated from the silicate Earth would, indeed, be enriched in light Nd isotopes. Similarly, another DFT study by Huang et al. (2019) also demonstrated that Ca in oldhamite is isotopically lighter than in silicates like forsterite, diopside or anorthite.

In order to understand the effect of the segregation of the Earth's core on the isotopic composition of the BSE, a mass balance model using the isotope fractionation factors for Nd in oldhamite and Nd in monazite at 1826.85 °C (2100 K) to approximate the conditions of Earth's latest core formation has been created following (Fig. 8):

$$\delta^{146}Nd_{Core} = \delta^{146}Nd_{Chondirte} - \frac{10^3 ln\alpha_{Monazite-Oldhamite} \times f_{BSE}}{100} \quad (14)$$

$$\delta^{146}Nd_{BSE} = \delta^{146}Nd_{Chondirte} - \frac{10^3 ln\alpha_{Oldhamite-Monazite} \times f_{Core}}{100} \quad (15)$$

where f_{BSE} and f_{Core} are the Nd fractions in the two reservoirs based on a bulk concentration of 457 ppb (McDonough and Sun, 1995), the masses of the two reservoirs ($m_{Core} = 1.94 \times 10^{24}$ kg; $m_{BSE} = 4.03 \times 10^{24}$), and core-silicate partition coefficients D_{Nd} come from Bouhifd et al. (2015) and Wohlers and Wood (2017). For internal consistency, monazite was chosen to represent the silicate Earth because it has the closest force constant (499 N/m) to the experimental value of Nd in silicate glass (513 N/m; Hu et al. (2023a)). As stated above, agreements of *ab initio* calculations with NRIXS measurements were within 22 N/m in the study of Nie et al. (2021) and there is no evidence yet that the force constants of lanthanides in silicate glass are dependent on the melt composition (Hu et al., 2023b). In absence of S, Nd would be extremely incompatible with experimental metal-silicate partition coefficients ranging from 0.00004 to 0.00056 (Bouhifd et al., 2015). Under oxidizing conditions, the highest experimental metal-silicate partition coefficient for Nd (0.001) requires a proportion of 24 % S in the Earth's core which is implausible for Solar System bodies. Under reducing conditions, the metal-silicate partition coefficients are orders of magnitudes higher when S is present (up to 0.30; Wohlers and Wood (2017)), In this scenario the bulk of Nd in the core will be hosted in a S-phase, therefore, the behaviour of Nd in the core can be approximated by a sulfide phase like oldhamite. The mass balance model in Fig. 8 demonstrates that only unrealistically high partition coefficients (>1; this would require highly reducing conditions) between the two reservoirs could generate a mantle composition distinguishable from chondrites. Therefore, the δ^{146}Nd composition of the BSE can be expected to be chondritic. Even reducing conditions, which would increase D_{Nd} drastically, would not result in a mantle composition significantly different from a chondritic composition (Fig. 8). This modelling agrees with evidence from other refractory lithophile elements which suggests insignificant incorporation into the Earth's core (McDonough and Sun, 1995; Palme et al., 2014).

4.3. Nd isotope fractionation during solar nebula condensation

Neodymium isotopes have long been used to understand the evolution of planetary bodies (DePaolo and Wasserburg, 1976; Norman, 1999; Nyquist et al., 1995). The refractory nature of REE made them condense quickly into primitive material from the cooling solar nebula (Lodders, 1996). Lanthanides are enriched in calcium-aluminium-rich inclusions (CAI) along with other refractory elements which makes CAI the earliest condensates in the Solar System. The isotopic composition of CAI can thus provide insights whether they formed in equilibrium with the nebular gas or by kinetic processes. Similar to the other lanthanides, Nd is proposed to have been present in a gas state in the solar nebula in different oxidation states but mostly as NdO molecules and a small proportion as atomic Nd^0 (Davis and Grossman, 1979). Here, the equilibrium fractionation of Nd between NdO gas and its precipitation in perovskite ($CaTiO_3$) in CAI has been modelled (Fig. 9a). Hibonite and notably perovskite are the main lanthanide hosting minerals in CAI (Davis and Grossman, 1979; Lodders, 2003). Given Nd substitutes Ca in hibonite (Kennedy et al., 1994) like in perovskite, the force constant of Nd in hibonite can be expected to be comparable to perovskite and thus this modelling approximates all condensed matter that hosts the bulk of Nd in CAI. As shown in Fig. 9a, the mass-dependent component of isotope fractionation becomes insignificant above ca. 500 °C (<0.006 ‰) with total fractionation dominated by the NFS effect which enriches perovskite in lighter isotopes. Total Nd isotope fractionation can be expected to be above currently achievable analytical uncertainties at temperatures > 1200 °C. At the formation temperature of perovskite (ca. 1376 °C; Boynton (1975)) which is only slightly above the 50 % condensation temperature of Nd (1328.85 °C; Lodders (2003)),

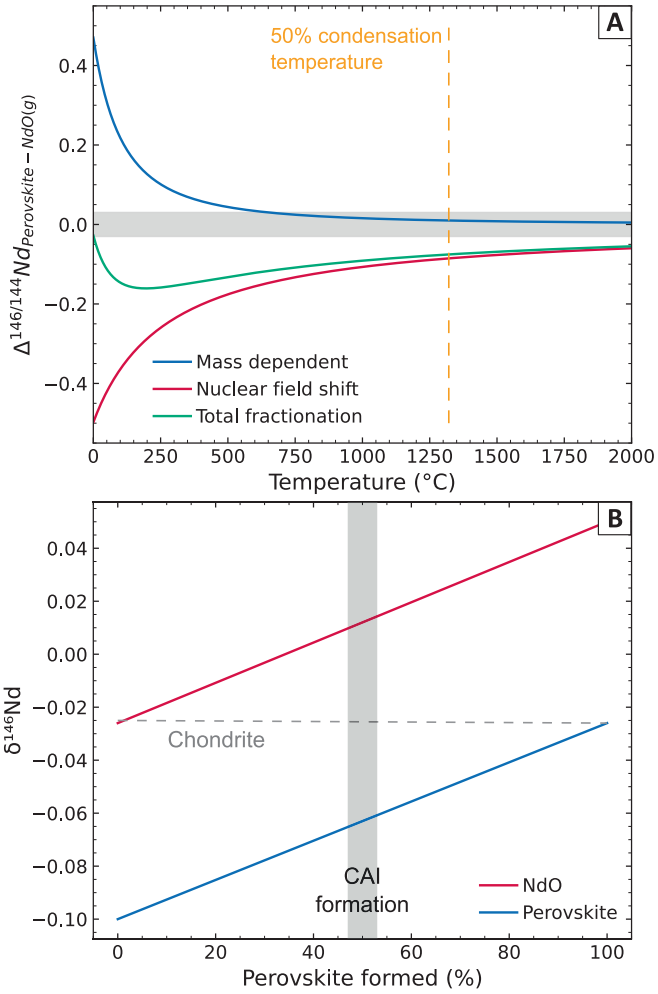

Fig. 9. Modelled equilibrium fractionation of $^{146}Nd/^{144}Nd$ during solar nebula condensation. (A) Equilibrium fractionation between gaseous NdO and condensed Nd in perovskite is dominated by the mass-independent nuclear field shift effect at temperatures relevant for the formation temperature of calcium-aluminium-rich inclusions (CAIs) (~1300 °C) and enriches the lighter isotope in the condensate. The grey area represents currently achievable analytical uncertainties (0.03 ‰). (B) Equilibrium fractionation can explain values of around –0.060 ‰ in CAIs but not the range of –1.86 to 2.20 ‰ observed in natural samples (Hu et al., 2021) assuming condensation around the 50 % condensation temperature of Nd (1328 °C) relevant for CAIs formation.

we would expect a δ^{146}Nd composition in CAI of ca. −0.06 ‰ (Fig. 9b) assuming a chondritic composition (–0.027 ± 0.005 ‰) of the initial solar nebula. The homogeneous composition of chondrites (McCoy-West et al., 2017) points towards limited heterogeneities in the solar nebula. Neodymium is not fully condensed after CAI formation (Boynton, 1975), thus a chondritic value cannot be expected in CAI. A study by Hu et al. (2021) reports δ^{146}Nd stable compositions in CAI which range from −0.93 to +1.1 ‰/amu which corresponds to −1.86 to +2.20 ‰ for δ^{146}Nd. These values are from pristine fine-grained CAI which are proposed to not have undergone further melting and vaporization after formation. This range of isotopic compositions is 10x greater than the entire range of δ^{146}Nd reported from terrestrial samples which range from −0.152 ‰ to +0.210 ‰ (Bai et al., 2023b). The huge range in isotopic composition found in CAI cannot be explained by equilibrium fractionation from a homogeneous nebular gas. Equilibrium fractionation has been excluded in previous studies to explain the isotopic composition of lanthanides in CAIs which agrees with the finding herein (Hu et al., 2021; Schauble, 2023). A kinetic origin of the isotopic composition of lanthanides in CAIs has been discussed (Hu et al., 2021) but also electromagnetic effects have been suggested (Moynier et al., 2006). Another study by Hu et al. (2025) demonstrated that Nd isotope ratios in CAI show mass-independent isotopic anomalies related to nucleosynthesis which excludes equilibrium fractionation. Further discussion here is beyond the scope of this work.

5. Summary

This study provides theoretical isotope fractionation factors for various Nd minerals and molecules applicable to a range of geological environments. The key findings are as follows:

1) Mass-dependent isotope fractionation of Nd is minimal between LREE enriched accessory minerals (e.g. monazite and apatite), but larger when Nd substitutes into Ca and Mg bearing minerals common in mafic systems (e.g. clinopyroxene and olivine). In zircon, Nd is exceptionally heavy.
2) The NFS effect shows much smaller fractionation among Nd^{3+}-species but a large inverse fractionation between Nd^{2+} and Nd^{3+} species. Nd^{2+}-species are isotopically lighter than Nd^{3+}-species contrary to the mass-dependent effect.
3) MORB and OIB resemble the δ^{146}Nd composition of chondrites while peridotites and komatiites are potentially superchondritic. As the bulk of Nd is hosted in clinopyroxene in mantle rocks and isotopically lighter clinopyroxene preferentially melts during mantle melting, an isotopically heavier mantle residuum is plausible, but the isotope fractionation cannot be quantified here. In addition, based on experimental data of Nd in silicate glass available, it can be inferred that the isotope fractionation between the mantle and the silicate melt will be insignificant.
4) A superchondritic composition of ultramafic rocks could also be explained by a reservoir of light Nd preferably in the Earth's core which agrees with the lighter force constant of S-bearing phases compared to silicates. However, because the Earth's core is not a significant host for Nd, the bulk silicate Earth can be expected to have a chondritic composition. This does not agree with mantle rocks being superchondritic and a more comprehensive analysis of the δ^{146}Nd composition of the mantle is required.
5) In terrestrial environments, Nd only occurs in the 3+ oxidation state which makes the mass-independent NFS effect negligible. However, under solar nebula conditions, Nd^{2+} in NdO condenses into primitive material during oxidation to Nd^{3+}. The NFS effect dominates the isotope fractionation at elevated temperatures during redox reactions by enriching the Nd^{3+}-phase in lighter isotopes in contrast to the mass-dependent effect. However, measured δ^{146}Nd isotope signatures found in refractory inclusions cannot be explained by equilibrium fractionation alone.

CRediT authorship contribution statement

Mark Nestmeyer: Writing – original draft, Visualization, Methodology, Data curation, Conceptualization. **Alex J. McCoy-West:** Writing – review & editing, Visualization, Supervision, Funding acquisition, Conceptualization.

Declaration of competing interest

The authors declare that they have no known competing financial interests or personal relationships that could have appeared to influence the work reported in this paper.

Acknowledgements

This study was supported by high performance computer resources at Pawsey Supercomputing Centre and James Cook University. We thank Dave Sherman for assisting with the methodology. This project was supported by ARC grant DE210101395 to AMW. We thank Paolo Sossi and two anonymous reviewers for thought provoking reviews and Marc Blanchard for the editorial handling.

Appendix A. Supplementary material

Table S1 shows the substitution mechanisms for the modelled minerals. Table S2 contains energy shifts and fermi contact densities of the Nd calibration molecules for the $^{146}Nd/^{144}Nd$ ratio. Table S3 shows polynomial coefficients for all Nd species which can be used to calculate $10^3 ln\beta$ values for the mass-dependent and nuclear field shift fractionation at a specific temperature. Table S4 displays nuclear charge radii ($\delta<r^2>$) and mass differences in amu for all possible stable Nd isotope pairs. Table S5 contains δ^{146}Nd compositions of igneous rocks compiled from the literature.

Supplementary material to this article can be found online at https://doi.org/10.1016/j.gca.2026.03.022.

Data availability

Data are available through Research Data JCU at https://doi.org/10.25903/mwn3-6t96.

References

Allegre, C.J., Poirier, J.-P., Humler, E., Hofmann, A.W., 1995. The chemical composition of the Earth. Earth Planet. Sci. Lett. 134 (3–4), 515–526.
Angeli, I., Marinova, K.P., 2013. Table of experimental nuclear ground state charge radii: an update. At. Data Nucl. Data Tables 99 (1), 69–95.
Ayers, J.C., Dittmer, S.K., Layne, G.D., 1997. Partitioning of elements between peridotite and H2O at 2.0–3.0 GPa and 900–1100 C, and application to models of subduction zone processes. Earth Planet. Sci. Lett. 150 (3–4), 381–398.
Bai, J., et al., 2025. Stable Nd isotopic fractionation in REY-rich deep-sea sediments. Earth Planet. Sci. Lett. 652.
Bai, J., et al., 2023a. High intermediate precision Sm isotope measurements in geological samples by MC-ICP-MS. J. Anal. At. Spectrom 38 (3), 629–637.
Bai, J., et al., 2021. Simultaneous measurement stable and radiogenic Nd isotopic compositions by MC-ICP-MS with a single-step chromatographic extraction technique. J. Anal. At. Spectrom 36 (12), 2695–2703.
Bai, J., et al., 2023b. Stable neodymium isotopic fractionation during chemical weathering. Earth Planet. Sci. Lett. 617.
Bai, J., et al., 2022. Stable neodymium isotope ratios of geological reference materials. Geostand. Geoanal. Res. 46 (4), 825–836.
Becke, A., 1993. Density-functional thermochemistry. III. The role of exact exchange. Chem. Phys. 98, 5648.
Bigeleisen, J., 1955. Statistical mechanics of isotopic systems with small quantum corrections. I. General considerations and the rule of the geometric mean. J. Chem. Phys. 23 (12), 2264–2267.
Bigeleisen, J., 1996. Nuclear size and shape effects in chemical reactions. Isotope chemistry of the heavy elements. J. Am. Chem. Soc. 118 (15), 3676–3680.
Bigeleisen, J., Mayer, M.G., 1947. Calculation of equilibrium constants for isotopic exchange reactions. J. Chem. Phys. 15 (5), 261–267.
Bindeman, I.N., Davis, A.M., 2000. Trace element partitioning between plagioclase and melt: investigation of dopant influence on partition behavior. Geochim. Cosmochim. Acta 64 (16), 2863–2878.

Bouhifd, M.A., et al., 2015. Superchondritic Sm/Nd ratio of the earth: impact of earth's core formation. Earth Planet. Sci. Lett. 413, 158–166.
Boyet, M., et al., 2018. Enstatite chondrites EL3 as building blocks for the Earth: the debate over the 146Sm–142Nd systematics. Earth Planet. Sci. Lett. 488, 68–78.
Boyet, M., Carlson, R.W., 2005. 142Nd evidence for early (>4.53 Ga) global differentiation of the silicate earth. Science 309 (5734), 576–581.
Boynton, W.V., 1975. Fractionation in the solar nebula: condensation of yttrium and the rare earth elements. Geochim. Cosmochim. Acta 39 (5), 569–584.
Burnham, A.D., O'Neill, H.S.C., 2020. Mineral–melt partition coefficients and the problem of multiple substitution mechanisms: insights from the rare earths in forsterite and protoenstatite. Contrib. Miner. Petrol. 175 (1), 7.
Chen, X., Wang, W., Zhang, Z., Nie, N.X., Dauphas, N., 2020. Evidence from *ab initio* and transport modeling for diffusion-driven zirconium isotopic fractionation in igneous rocks. ACS Earth Space Chem. 4 (9), 1572–1595.
Coey, J., Ghatak, S., Avignon, M., Holtzberg, F., 1976. Electronic configuration of samarium sulphide and related compounds: Mössbauer-effect measurements and a model. Phys. Rev. B 14 (9), 3744.
Crozaz, G., Lundberg, L.L., 1995. The origin of oldhamite in unequilibrated enstatite chondrites. Geochim. Cosmochim. Acta 59 (18), 3817–3831.
Davis, A.M., Grossman, L., 1979. Condensation and fractionation of rare earths in the solar nebula. Geochim. Cosmochim. Acta 43 (10), 1611–1632.
de La Rocha, C.L., Brzezinski, M.A., DeNiro, M.J., 1997. Fractionation of silicon isotopes by marine diatoms during biogenic silica formation. Geochim. Cosmochim. Acta 61 (23), 5051–5056.
DePaolo, D.J., 2012. Neodymium Isotope Geochemistry: An Introduction. Springer Science & Business Media, p. 20.
DePaolo, D.J., Wasserburg, G., 1976. Nd isotopic variations and petrogenetic models. Geophys. Res. Lett. 3 (5), 249–252.
Dickinson, T.L., McCoy, T.J., 1997. Experimental rare-earth-element partitioning in oldhamite: implications for the igneous origin of aubritic oldhamite. Meteorit. Planet. Sci. 32 (3), 395–412.
Dohmen, R., Blundy, J., 2014. A predictive thermodynamic model for element partitioning between plagioclase and melt as a function of pressure, temperature and composition. Am. J. Sci. 314 (9), 1319–1372.
Dolg, M., Stoll, H., Preuss, H., 1993. A combination of quasirelativistic pseudopotential and ligand field calculations for lanthanoid compounds. Theor. Chim. Acta 85, 441–450.
Downs, R.T., Hall-Wallace, M., 2003. The American Mineralogist crystal structure database. Am. Mineral. 88 (1), 247–250.
Duan, H., Huang, F., 2024. Equilibrium indium isotope fractionation between indium-bearing minerals: insights from first-principles calculations. Geochim. Cosmochim. Acta 369, 51–61.
Eibschütz, M., Cohen, R., Buehler, E., Wernick, J., 1972. Mössbauer isomer shifts in Sm 149 compounds. Phys. Rev. B 6 (1), 18.
Erba, A., et al., 2022. CRYSTAL23: a program for computational solid state physics and chemistry. J. Chem. Theory Comput. 19 (20), 6891–6932.
Feng, C., Qin, T., Huang, S., Wu, Z., Huang, F., 2014. First-principles investigations of equilibrium calcium isotope fractionation between clinopyroxene and Ca-doped orthopyroxene. Geochim. Cosmochim. Acta 143, 132–142.
Finch, R.J., Hanchar, J.M., Hoskin, P.W., Burns, P.C., 2001. Rare-earth elements in synthetic zircon: part 2. A single-crystal X-ray study of xenotime substitution. Am. Mineral. 86 (5–6), 681–689.
Fricke, G., Heilig, K., Schopper, H.F., 2004. Nuclear Charge Radii. Springer, Berlin.
Frossard, P., Israel, C., Bouvier, A., Boyet, M., 2022. Earth's composition was modified by collisional erosion. Science 377 (6614), 1529–1532.
Goethals, J., Bedidi, A., Fourdrin, C., Tarrida, M., Rossano, S., 2019. Experimental study of trivalent rare-earth element incorporation in $CaTiO_3$ perovskite: evidence for a new substitution mechanism. Phys. Chem. Miner. 46, 1003–1015.
Gomes, A.S., Dyall, K.G., Visscher, L., 2010. Relativistic double-zeta, triple-zeta, and quadruple-zeta basis sets for the lanthanides La–Lu. Theor. Chem. Acc. 127, 369–381.
Gonze, X., et al., 2020. The Abinit project: impact, environment and recent developments. Comput. Phys. Commun. 248, 107042.
Gražulis, S., et al., 2009. Crystallography open database–an open-access collection of crystal structures. Appl. Crystallogr. 42 (4), 726–729.
Green, D., Ringwood, A., 1967. The genesis of basaltic magmas. Contrib. Miner. Petrol. 15, 103–190.
Hanchar, J.M., et al., 2001. Rare earth elements in synthetic zircon: part 1. Synthesis, and rare earth element and phosphorus doping. Am. Mineral. 86 (5–6), 667–680.
Hu, J.Y., et al., 2021. Heating events in the nascent solar system recorded by rare earth element isotopic fractionation in refractory inclusions. Sci. Adv. 7 (2).
Hu, J.Y., et al., 2025. Rare earth element nucleosynthetic anomalies and dust transport in the protoplanetary disk. Sci. Adv. 11 (28), eadv3148.
Hu, J.Y., et al., 2023a. Determination of rare earth element isotopic compositions using sample-standard bracketing and double-spike approaches. ACS Earth Space Chem. 7 (11), 2222–2238.
Hu, Y., et al., 2023b. Equilibrium fractionation of REE isotopes in nature: insights from NRIXS and DFT+ U studies of Eu and Dy phonon density of states. Geochim. Cosmochim. Acta 348, 323–339.
Huang, F., Zhou, C., Wang, W., Kang, J., Wu, Z., 2019. First-principles calculations of equilibrium Ca isotope fractionation: implications for oldhamite formation and evolution of lunar magma ocean. Earth Planet. Sci. Lett. 510, 153–160.
Hyung, E., Ibañez-Mejia, M., Rojas-Agramonte, Y., 2023. The survival of tracers of primordial mantle heterogeneity investigated through $^{142}Nd/^{144}Nd$ and 3He/4He isotope decoupling in the Gorgona Island lavas. Earth Planet. Sci. Lett. 622, 118409.
Jain, A., et al., 2013. Commentary: the materials project: a materials genome approach to accelerating materials innovation. APL Mater. 1 (1).
Jollet, F., Torrent, M., Holzwarth, N., 2014. Generation of projector augmented-wave atomic data: a 71 element validated table in the XML format. Comput. Phys. Commun. 185 (4), 1246–1254.
Kaindl, G., 1970. Mössbauer effect study of hyperfine interactions in 145 Nd. Zeitschrift Für Physik A Hadrons and Nuclei 240, 100–122.
Kaufmann, A.K., McCoy-West, A.J., 2025. Combined stable and radiogenic Nd isotope characterisation of sedimentary and iron formation reference materials by double spike MC-ICP-MS. Geostand. Geoanal. Res.
Kennedy, A., Lofgren, G., Wasserburg, G., 1994. Trace-element partition coefficients for perovskite and hibonite in meteorite compositions. Chem. Geol. 117 (1–4), 379–390.
Knyazev, D.A., Myasoedov, N.F., 2001. Specific effects of heavy nuclei in chemical equilibrium. Sep. Sci. Technol. 36 (8–9), 1677–1696.
Lee, C., Yang, W., Parr, R.G., 1988. Development of the Colle-Salvetti correlation-energy formula into a functional of the electron density. Phys. Rev. B 37 (2), 785.
Li, Y., Hardin, J., Wang, W., Wu, Z., Huang, S., 2025. Mineral-melt calcium isotope fractionation factors constrained using ab initio molecular dynamics simulations and their implications to calcium isotope effects during partial melting in the upper mantle. Geochim. Cosmochim. Acta 396, 51–70.
Litasov, K.D., Shatskiy, A., 2016. Composition of the earth's core: a review. Russ. Geol. Geophys. 57 (1), 22–46.
Liu, F., et al., 2023a. Simultaneously obtaining stable and radiogenic Nd isotope ratios through a single DGA column using double spike TIMS. J. Anal. At. Spectrom 38 (12), 2581–2589.
Liu, F., et al., 2023b. Stable cerium isotope analysis of geological materials by MC-ICP-MS. Chem. Geol.
Lodders, K., 1996. An experimental and theoretical study of rare-earth-element partitioning between sulfides (FeS, CaS) and silicate and applications to enstatite achondrites. Meteorit. Planet. Sci. 31 (6), 749–766.
Lodders, K., 2003. Solar system abundances and condensation temperatures of the elements. Astrophys. J. 591 (2), 1220.
Ma, Z., Wang, W., Wang, S.-J., 2024. First-principles calculations of equilibrium inter-mineral nickel isotope fractionation in the mantle. Lithos 490, 107848.
McCoy-West, A.J., Burton, K.W., Millet, M.-A., Cawood, P.A., 2021. The chondritic neodymium stable isotope composition of the earth inferred from mid-ocean ridge, ocean island and arc basalts. Geochim. Cosmochim. Acta 293, 575–597.
McCoy-West, A.J., Millet, M.-A., Burton, K.W., 2017. The neodymium stable isotope composition of the silicate Earth and chondrites. Earth Planet. Sci. Lett. 480, 121–132.
McCoy-West, A.J., Millet, M.-A., Burton, K.W., 2020a. The neodymium stable isotope composition of the oceanic crust: reconciling the mismatch between erupted mid-ocean ridge basalts and lower crustal gabbros. Front. Earth Sci. 8.
McCoy-West, A.J., Millet, M.-A., Nowell, G.M., Nebel, O., Burton, K.W., 2020b. Simultaneous measurement of neodymium stable and radiogenic isotopes from a single aliquot using a double spike. J. Anal. At. Spectrom 35 (2), 388–402.
McCoy-West, A.J., Mortimer, N., Burton, K.W., Ireland, T.R., Cawood, P.A., 2022. Re-initiation of plutonism at the Gondwana margin after a magmatic hiatus: the bimodal Permian-Triassic Longwood Suite, New Zealand. Gondw. Res. 105, 432–449.
McDonough, W., 2003. Compositional Model for the Earth's Core, The Mantle and Core. Elsevier Inc., pp. 547–568
McDonough, W.F., Sun, S.-S., 1995. The composition of the earth. Chem. Geol. 120 (3–4), 223–253.
Moynier, F., et al., 2006. Europium isotopic variations in Allende CAIs and the nature of mass-dependent fractionation in the solar nebula. Geochim. Cosmochim. Acta 70 (16), 4287–4294.
Moynier, F., Yin, Q.-Z., Schauble, E., 2011. Isotopic evidence of Cr partitioning into earth's core. Science 331 (6023), 1417–1420.
Nakada, R., Tanimizu, M., Takahashi, Y., 2013. Difference in the stable isotopic fractionations of Ce, Nd, and Sm during adsorption on iron and manganese oxides and its interpretation based on their local structures. Geochim. Cosmochim. Acta 121, 105–119.
Nestmeyer, M., McCoy-West, A.J., 2025. Quantifying mass-dependent isotope fractionation and nuclear field shift effects for the light rare Earth elements in hydrous systems. Geochim. Cosmochim. Acta 388, 236–252.
Nicol, L., Garçon, M., Boyet, M., Gannoun, A., 2023. High-precision measurement of europium isotopic composition of geological reference materials by multi-collector inductively coupled plasma mass spectrometry (MC-ICP-MS). J. Anal. At. Spectrom. 38 (6), 1261–1274.
Nie, N.X., et al., 2021. Iron, magnesium, and titanium isotopic fractionations between garnet, ilmenite, fayalite, biotite, and tourmaline: results from NRIXS, ab initio, and study of mineral separates from the Moosilauke metapelite. Geochim. Cosmochim. Acta 302, 18–45.
Norman, M.D., 1999. The composition and thickness of the crust of Mars estimated from rare earth elements and neodymium-isotopic compositions of Martian meteorites. Meteorit. Planet. Sci. 34 (3), 439–449.
Nyquist, L., et al., 1995. 146Sm-142Nd formation interval for the lunar mantle. Geochim. Cosmochim. Acta 59 (13), 2817–2837.
Palme, H., O'Neill, H.S.C., Holland, H., Turekian, K., 2014. In: Treatise on Geochemistry. Elsevier, Amsterdam, pp. 1–39.
Pan, Y., Fleet, M.E., 2002. Compositions of the apatite-group minerals: substitution mechanisms and controlling factors. Rev. Mineral. Geochem. 48 (1), 13–49.
Perdew, J.P., Burke, K., Ernzerhof, M., 1996. Generalized gradient approximation made simple. Phys. Rev. Lett. 77 (18), 3865.

Piepgras, D.J., Wasserburg, G., 1980. Neodymium isotopic variations in seawater. Earth Planet. Sci. Lett. 50 (1), 128–138.
Pourkhorsandi, H., Debaille, V., Armytage, R.M., de Jong, J., 2024. Cerium stable isotopic composition of non-carbonaceous chondrites. ACS Earth Space Chem. 8 (12), 2452–2462.
Pourkhorsandi, H., Debaille, V., de Jong, J., Armytage, R.M.G., 2021. Cerium stable isotope analysis of synthetic and terrestrial rock reference materials by MC-ICPMS. Talanta 224, 121877.
Rabin, S., Blanchard, M., Pinilla, C., Poitrasson, F., Grégoire, M., 2023. Iron and silicon isotope fractionation in silicate melts using first-principles molecular dynamics. Geochim. Cosmochim. Acta 343, 212–233.
Révillon, S., Arndt, N., Chauvel, C., Hallot, E., 2000. Geochemical study of ultramafic volcanic and plutonic rocks from Gorgona Island, Colombia: the plumbing system of an oceanic plateau. J. Petrol. 41 (7), 1127–1153.
Saji, N.S., Wielandt, D., Paton, C., Bizzarro, M., 2016. Ultra-high-precision Nd-isotope measurements of geological materials by MC-ICPMS. J. Anal. At. Spectrom. 31 (7), 1490–1504.
Saue, T., et al., 2020. The DIRAC code for relativistic molecular calculations. J. Chem. Phys. 152 (20), 204104.
Schauble, E.A., 2004. Applying stable isotope fractionation theory to new systems. Rev. Mineral. Geochem. 55 (1), 65–111.
Schauble, E.A., 2011. First-principles estimates of equilibrium magnesium isotope fractionation in silicate, oxide, carbonate and hexaaquamagnesium(2+) crystals. Geochim. Cosmochim. Acta 75 (3), 844–869.
Schauble, E.A., 2013. Modeling nuclear volume isotope effects in crystals. Proc. Natl. Acad. Sci. 110 (44), 17714–17719.
Schauble, E.A., 2023. Nuclear volume isotope fractionation of europium and other lanthanide elements. Geochem. J. 57 (4), 118–133.
Schauble, E.A., 2024. Nuclear volume and mass dependent fractionation of cerium isotopes. Geochem. J. 58 (6), 227–245.
Schoneveld, L., O'Neill, H.S.C., 2019. The influence of melt composition on the partitioning of trace elements between anorthite and silicate melt. Contrib. Miner. Petrol. 174 (2), 13.
Schosnig, M., Hoffer, E., 1998. Compositional dependence of REE partitioning between diopside and melt at 1 atmosphere. Contrib. Miner. Petrol. 133 (3), 205–216.
Seifert, W., 2005. REE-, Zr-, and Th-rich titanite and associated accessory minerals from a kersantite in the Frankenwald, Germany. Mineral. Petrol. 84, 129–146.
Sen, S., 2000. Atomic environment of high-field strength Nd and Al cations as dopants and major components in silicate glasses: a Nd LIII-edge and Al K-edge X-ray absorption spectroscopic study. J. Non Cryst. Solids 261 (1–3), 226–236.
Shannon, R.D., 1976. Revised effective ionic radii and systematic studies of interatomic distances in halides and chalcogenides. Found. Crystallogr. 32 (5), 751–767.
Sossi, P.A., Fegley Jr, B., 2018. Thermodynamics of element volatility and its application to planetary processes. Rev. Mineral. Geochem. 84 (1), 393–459.
Sun, C., Graff, M., Liang, Y., 2017. Trace element partitioning between plagioclase and silicate melt: the importance of temperature and plagioclase composition, with implications for terrestrial and lunar magmatism. Geochim. Cosmochim. Acta 206, 273–295.
Topsakal, M., Wentzcovitch, R., 2014. Accurate projected augmented wave (PAW) datasets for rare-earth elements (RE= La–Lu). Comput. Mater. Sci. 95, 263–270.
Umesh, B., et al., 2011. Synthesis and characterization of spherical and rod like nanocrystalline Nd2O3 phosphors. J. Alloy. Compd. 509 (4), 1146–1151.
Urey, H.C., 1947. The thermodynamic properties of isotopic substances. J. Chem. Soc. 562–581.
Vilela Oliveira, D., Laun, J., Peintinger, M.F., Bredow, T., 2019. BSSE-correction scheme for consistent gaussian basis sets of double-and triple-zeta valence with polarization quality for solid-state calculations. J. Comput. Chem. 40 (27), 2364–2376.
Visscher, L., Dyall, K.G., 1997. Dirac–Fock atomic electronic structure calculations using different nuclear charge distributions. At. Data Nucl. Data Tables 67 (2), 207–224.
Weigend, F., Ahlrichs, R., 2005. Balanced basis sets of split valence, triple zeta valence and quadruple zeta valence quality for H to Rn: design and assessment of accuracy. PCCP 7 (18), 3297–3305.
Winter, J.D., 2014. Principles of Igneous and Metamorphic Petrology. Pearson education Harlow, UK.
Wohlers, A., Wood, B.J., 2017. Uranium, thorium and REE partitioning into sulfide liquids: implications for reduced S-rich bodies. Geochim. Cosmochim. Acta 205, 226–244.
Wu, H., et al., 2024. A chromatographic approach for high-precision Eu isotope analysis. Anal. Chem. 96 (38), 15102–15107.
Yadav, D., Bura, N., Bhoriya, A., Singh, J., Sharma, N.D., 2021. Estimation of anharmonic parameters of nano-crystalline Sc_2O_3 and Nd_2O_3. Mater. Today Commun. 29, 102759.
Yang, J., Dolg, M., 2005. Valence basis sets for lanthanide 4f-in-core pseudopotentials adapted for crystal orbital ab initio calculations. Theor. Chem. Acc. 113, 212–224.
Zindler, A., Hart, S., 1986. Chemical geodynamics. In: Annual review of earth and planetary sciences. Volume 14 (A87-13190 03-46). Palo Alto, CA, Annual Reviews, Inc., 1986, p. 493-571., 14: 493-571.